Available online at www.sciencedirect.com
ScienceDirect
Journal of the European Ceramic Society 29 (2009) 2225–2234
www.elsevier.com/locate/jeurceramsoc

Investigation of sintering mechanisms of alumina using kinetic field and master sintering diagrams

F. Raether*, P. Schulze Horn

Fraunhofer Institut Silicatforschung ISC, Neunerplatz 2, D-97082 Würzburg, Germany

Received 29 July 2008; received in revised form 9 January 2009; accepted 19 January 2009
Available online 23 February 2009

Abstract

Strain rates during sintering of alumina at different heating rates between 0.2 and 20 K/min have been measured non-contact using a thermooptical measuring technique. The shrinkage data were represented in a kinetic field diagram. It was shown that coarsening effects can be indirectly derived from the position and slope of iso-strain lines identified in the kinetic field. In addition temperature gradients which frequently lead to an erroneous interpretation of shrinkage kinetics were identified. Uni-axial loads up to 6 MPa were applied during sintering. The strain rates were measured parallel and perpendicular to the load. They were processed in separate kinetic field diagrams. It was shown that creep leads to a parallel shift of the iso-strain lines either to lower temperatures, for the strain rates parallel to the load, or to higher temperatures, for the strain rates perpendicular to the load. The individual kinetic field diagrams for a specific load were assembled in 3d, with the load used as z-axis. They formed a master sintering diagram (MSD) where the iso-strain lines were replaced by iso-strain surfaces. The parallel shift of the iso-strain lines with load enabled a simple representation of sintering kinetics for various loads during the entire range of densification, temperatures and heating rates.

Keywords: Sintering kinetics; Activation energy; Alumina; Constrained sintering; Sinter forging; Kinetic field

1. Introduction

Numerous models have been proposed for a computer simulation of sintering using constitutive equations.[1,2] The accuracy of the models depends critically on the quality of the experimental data which are used as input for the simulation. The effect of additional stresses during sintering was primarily investigated by loading dilatometry (with small loads) and sinter forging tests (with large loads). During the heat treatment, strain rates were measured, when a uni-axial compressive load was applied. Either constant[3] or cyclic[4] loads were used. Preferentially, strain rates were measured parallel and perpendicular to the load direction. From the strain rates measured for different loads, the viscous Young moduli and Poisson ratios were derived.[5] These quantities were required in the constitutive equations used for simulating constrained sintering. They vary with temperature and porosity of the compacts.

The mechanisms which control microstructure changes during solid state sintering of ceramics were identified already in the middle of the last century.[6] Sintering shrinkage is driven by the surface energy of the porous compacts. Surface diffusion, grain boundary diffusion and volume diffusion are the main mechanisms for material transfer. Only the last two lead to shrinkage of the compacts, whereas surface diffusion increases the particle contacts and decreases surface curvature, thereby eliminating smaller grains and reducing sintering activity. The strain rate can be described by[6]:

$$-\frac{\mathrm{d}\varepsilon_f}{\mathrm{d}t} = \frac{1}{3\rho}\frac{\mathrm{d}\rho}{\mathrm{d}t} = \frac{C_1(\rho)\gamma D}{kTG^n}; \quad D = D_0 \exp\left(-\frac{Q}{RT}\right) \tag{1}$$

with ε_f = true strain, ρ = density, t = time, C_1 = constant depending on microstructure, γ = solid–gas interface energy, D = diffusion coefficient, Q = activation energy for diffusion mechanism leading to densification, R = gas constant, k = Boltzmann constant, T = absolute temperature, G = mean grain diameter, n = exponent depending on mechanism (3 for volume diffusion and 4 for grain boundary diffusion). Grain

* Corresponding author. Tel.: +49 931 4100 200.
E-mail address: friedrich.raether@isc.fraunhofer.de (F. Raether).

0955-2219/$ – see front matter © 2009 Elsevier Ltd. All rights reserved.
doi:10.1016/j.jeurceramsoc.2009.01.025

growth was described by[6]:

$$G^m = G_0^m + C_2(T)t; \quad C_2(T) = C_0(\rho)\ \exp\left(-\frac{Q_G}{RT}\right) \tag{2}$$

with G_0 = initial grain size, m = grain growth exponent – depending on mechanism, C_2 = constant depending on temperature and microstructure, C_0 = frequency factor depending on microstructure, Q_G = activation energy for grain growth.

Loading at high temperatures leads to creep which was attributed to various mechanisms, e.g. grain boundary or volume diffusion, dislocation climb or grain boundary sliding.[7–9] In all cases the creep rate depends in the same way on the diffusion coefficient, grain size and inverse temperature as the strain rate in Eq. (1). For a uni-axial compressive (i.e. negative) stress in z-direction σ_z the strain rate in the direction parallel to z becomes more negative and the strain rate in the lateral direction increases[5]:

$$\frac{d\varepsilon_z}{dt} = \frac{d\varepsilon_f}{dt} + \frac{1}{E_v}\sigma_z; \quad \frac{d\varepsilon_r}{dt} = \frac{d\varepsilon_f}{dt} - \frac{\nu_v}{E_v}\sigma_z \tag{3}$$

with indices z, r and f indicating strain rates parallel and perpendicular to the load direction and free sintering, respectively. E_v and ν_v are the uni-axial viscosity and the viscous Poisson coefficient, respectively. The viscous Poisson coefficient ν_v depends on density. The uni-axial viscosity E_v is given by[6]:

$$E_v^{-1} = \frac{C_3(\rho)\exp(-Q_c/RT)}{G^p kT} \tag{4}$$

with $C_3(\rho)$ = constant depending on microstructure, Q_c = activation energy for creep, G = grain size, p = grain size exponent depending on creep mechanism (e.g. $p = 2$ for Nabarro–Herring creep and $p = 3$ for Coble creep).[7,8]

From Eq. (1) it was concluded that solid state sintering can be described by a master sintering curve (MSC), if strain or density are plotted versus the time integral $\int D/T\, dt$.[10] It was shown that various heating cycles of one type of green compact were described by the same MSC. Since constant activation energy during the entire sintering process is not realistic for many technical ceramics, an extension of the MSC approach was suggested by Kiani et al. who fitted Q in several strain segments to consider changes in the activation energy during densification.[11] A 3d extension of the MSC approach was given by An and Johnson for the description of hot pressing, where the load was used as the z-axis.[12] On the other hand, an Arrhenius type diagram was introduced by Palmour already in 1988, to calculate the time temperature cycles required for rate controlled sintering (RCS).[13] This diagram was called kinetic field. It showed a logarithmic plot of densification rates, measured during sintering of green compacts with different constant heating rates, versus the reciprocal absolute temperature. Points of equal density on different shrinkage curves were connected to form so-called iso-density lines.[13] From Eq. (1) it becomes clear that the product of densification rate $d\rho/dt$ and associated absolute temperatures T depends on some microstructure parameters which vary slowly with temperature and on the diffusion coefficient which has exponential temperature dependence. Analogical to the kinetic field approach, the logarithm of the product $\ln(-T\, d\rho_f/dt)$ was plotted versus the inverse absolute temperature $1/T$[14] (compare Eq. (1)):

$$\ln\left(-T\frac{d\varepsilon_f}{dt}\right) = \ln\left(\frac{C_1(\rho)\gamma D_0}{k}\right) - n\ \ln G - \frac{Q}{R}\frac{1}{T} \tag{5}$$

where the symbols have the same meaning as in Eq. (1).

Instead of iso-density lines, iso-strain lines can be used.[15] They are formed by connecting points of equal strain on different sintering curves of the kinetic field diagram. (The iso-strain lines allow considering anisotropic shrinkage during loading experiments as shown below.) Usually straight lines were obtained for the iso-density and iso-strain lines, respectively. From the slope m of the lines, the activation energy Q for densification was calculated for the respective density according to:

$$m = -\frac{Q}{R}. \tag{6}$$

The time integral of densification rates interpolated from the iso-density lines was used to calculate the densification at arbitrary time temperature cycles.[16] By that, model free predictions of densification were obtained. For any time–temperature cycle leading to a density ρ at time t and temperature T a densification rate $d\rho/dt$ can be interpolated from the kinetic field using the two adjacent iso-density lines. With the heating rate β the temperature and density after a short time interval Δt are calculated:

$$T(t + \Delta t) = T(t) + \beta\Delta t; \quad \rho(t + \Delta t) = \rho(t) + \frac{d\rho}{dt}\Delta t. \tag{7}$$

Subsequent iterations allow for the calculation of densification curves for arbitrary time–temperature cycles. Vice versa, the time–temperature cycle can be calculated which provides prescribed densification rates. The later was used for RCS.[13,16] It is pointed out that the kinetic field diagram is unique for a special type of green sample. If particle size, green density or any other parameter affecting sintering kinetics is changed, the corresponding shrinkage curves have to be measured again and the diagram has to be rebuild.

Alumina is the most important technical ceramic and its composition is comparatively simple. Therefore its sintering behaviour was investigated since the early work of Coble and Kingery five decades ago. Now it is assumed that densification is controlled by lattice diffusion of the Al^{3+} cations with an activation energy $Q = 580$ kJ/mol.[6] Coarsening is attributed to surface diffusion with activation energies in the range of 230–280 kJ/mol.[6] With this interpretation the exponents n and m (compare Eqs. (1) and (2)) are 3 and 4, respectively. Often densification in alumina is also attributed to a control by grain boundary diffusion (compare e.g. Ref. [17]) which reflects difficulties in reproducing green samples and performing accurate measurements. The activation energy for grain growth in dense alumina is 440 kJ/mol.[9,17] A similar activation energy of 460 kJ/mol was found for plastic deformation of dense alumina.[18] In porous alumina a larger apparent activation energy for grain growth of 690 kJ/mol was found which was attributed to the decrease of grain boundary mobility by pore drag.[9,19] Different results were obtained for the relation between average grain size and density. If homogenous green samples were prepared –

e.g. by colloidal methods – the onset of grain growth occurred in a late stage of densification above a fractional density of 90%.[14] Using customary forming processes also grain growth in the intermediate sintering stage was observed.[20] Recently it was shown that the loading history strongly altered viscous moduli and strain rates during isothermal sintering of alumina.[21] Negative Poisson ratios were observed after prolonged loading and anisotropic strain was measured in free sintering after removal of a previously applied stress. This was explained by the formation of anisotropic microstructure during loading. For uni-axial compressive stresses, prolate pores oriented parallel to the load were formed.[21]

In the present paper a thermooptical measuring method was used which allowed the in situ measurement of axial and lateral strains during the entire heating cycle. The kinetic field method was extended to a 3d representation of the data at different loads. Various effects which control sintering kinetics and microstructure changes during free sintering and sinter forging were measured with alumina green samples.

2. Experimental

2.1. Sample preparation

Green samples were prepared from an ultrapure (>99.99%) alumina powder (Taimicron TM-DAR) with a particle size d_{50} of 0.2 μm. Cylindrical compacts (diameter 20 mm and height 50 mm) were formed by cold isostatic pressing at a pressure of 500 MPa. No additives were used. The compacts were turned to a diameter of 6.5 and 11 mm for loaded and free sintering, respectively. Then they were cut by a diamond saw to obtain parallel faces with a height of 17 mm for loaded sintering and 11 mm for free sintering. (The larger aspect ratio for loading experiments was chosen to obtain larger axial strain rates.) Green density was 58% of theoretical density. Samples used in sinter forging experiments were preheated at 1000 °C for 1 h prior to sintering to increase their strength.

Partially sintered samples were used to investigate the microstructural changes during sintering. These samples were prepared by constant rate heating with 0.5 K/min, subsequent quenching to ambient temperature when a predefined strain was achieved, polishing and thermal etching for 30 min at 50 K below the maximum temperature of the constant rate heating cycle. The microstructure was examined in a scanning electron microscope (SEM Zeiss Ultra, Oberkochen, Germany). The homogeneity of the pore distribution was measured according to a variance analysis method described by Missiaen and Thomas.[22] For that, the SEM images were converted to binary images and the pore fraction p was determined in several quadratic sections with predefined edge length l_s. The variance σ^2 of the pore fraction when comparing different sections was scaled by the variance σ^2_{ran} that was expected for a 2d random distribution of pores according to:

$$\frac{\sigma^2}{\sigma^2_{ran}} = \frac{\sigma^2 l_s^2}{p l_p^2} \quad (8)$$

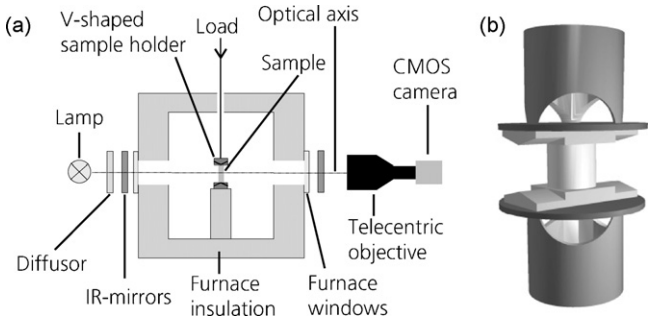

Fig. 1. Sketch of the thermooptical measuring device TOMMI (a); set-up with V-shaped punches used for loading dilatometry (b).

with l_p average chord length of pores determined by lineal intercept analysis. The scaled variance was calculated from several SEM images for sections with different edge length and plotted versus the edge length of the sections. Straight lines were obtained where the slope is a measure of the homogeneity.[22] Densities of green and sintered samples were measured by the Archimedian method.

2.2. In situ measuring technique

Dimensional changes during sintering were measured, using a thermooptical measuring device (TOMMI).[15,23] Its chamber kiln was operated in air and heated by $MoSi_2$ heating elements. Images from the sample were obtained, using the illumination from a halogen lamp, a diffuser, a telecentric objective and a CMOS camera (Fig. 1a). Details of the set-up are presented in Ref. [15]. Fig. 2 shows the thermal expansion of a sintered alumina sample measured by TOMMI. Different from customary push-rod dilatometry, no correction of the data was required. The measured data were in close agreement to literature values which demonstrated that the accuracy of dimension measurement was sufficient for the kinetic studies presented below.

Sintering was performed either without load with the sample placed on an alumina substrate (10 mm thick, 43 mm long

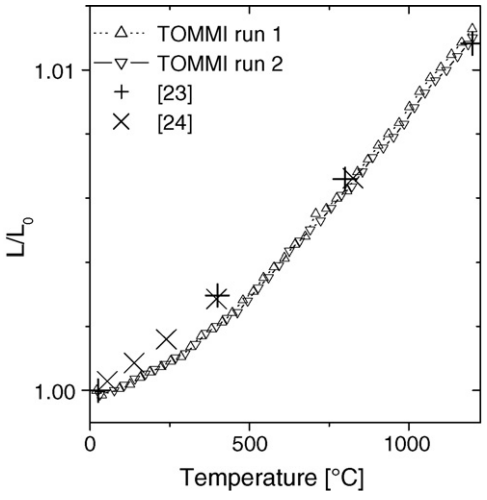

Fig. 2. Scaled width L/L_0 of a sintered alumina sample during heating with 10 K/min in TOMMI compared to thermal expansion data from Refs. [24,25].

and 10 mm wide) or with a load which was applied via vertical punches. During loaded sintering loads varied between 1 and 180 N, corresponding to a compressive stress between 0.03 and 5.4 MPa. (The minimum load of 1 N was required to maintain the contact between punches and sample. The 1 N runs were used for comparing with runs using higher loads without changing the temperature distribution of the set-up.) The punches were made of alumina. They had lateral extensions with a V-shaped cross-section to allow for an accurate measurement of sample height even if a small tilting of the set-up occurred during the heat treatment (Fig. 1b). Sample height in loading dilatometry experiments was extracted from the vertical distance of the edges of upper and lower punch, interpolated at the centre of the sample. Sample width was measured by averaging the horizontal distance of the contour lines in the intermediate third of the sample. Platinum alloy foils were used as an interlayer between samples and punches to reduce caking and friction during sintering. By that it was made sure that the deformation of the cylindrical sample during sinter forging was small. Deviations from cylindrical geometry were measured at different heights by the optical system. Due to friction at the punches, sample width near the punches was up to 5% larger than in the centre region. This leads to a difference up to 2% when sample volumes were calculated either from the entire silhouette – assuming an axi-symmetric geometry – or from width and height – assuming cylindrical geometry.

Samples were heated with a heating rate of 10 K/min to 890 and 1000 °C for free sintering and loaded sintering, respectively. Then, for loaded sintering experiments a holding period of 3 h was introduced. This holding period allowed for some creep to obtain an accurate match of the load bearing faces of the sample to the punches. Thereafter, the samples were sintered with different heating rates between 0.2 and 20 K/min. Maximum temperature was increased with increasing heating rate from 1225 to 1400 °C to cover a large area in the kinetic field diagrams. Holding time at maximum temperature was 2 h for free sintering and 3 h for loaded sintering, respectively. Temperature calibration was performed by the optical measurement of the melting of gold sheet (purity > 99.99) which was placed in a hole drilled in an alumina sample. In addition, pyrometric rings made of alumina (type PTCR-HTH, dmc^2 electronic materials B.V., Uden, the Netherlands) were used for the temperature calibration at higher temperatures.

The measured data, i.e. width and height of the cylindrical samples, were corrected for thermal expansion. Thermal expansion was obtained from fitting a second order polynomial to the measured thermal expansion curve of a sintered alumina sample heated in the same set-up (compare Fig. 2). Then the data were scaled to their respective dimension measured at 900 °C for free sintering and 170 min after the beginning of the holding period at 1000 °C for loaded sintering, respectively. By that, all deviations due to settling of the samples were eliminated.

Thermal diffusivity of alumina samples was measured by the laser flash method. The device was described in Ref. [26]. An alumina green sample which was heated up to 1175 °C with 20 K/min and quenched thereafter showed a thermal diffusivity of 2.0×10^{-6} m^2/s which is about 20% of the thermal diffusivity of dense alumina at ambient temperature. The temperature gradients during heating of the alumina samples were simulated using this ratio r and a polynomial fit of inverse thermal diffusivity of a dense alumina sample measured in the temperature range between ambient temperature and 1600 °C:

$$k = \frac{r}{8.326 \times 10^{-8} + 7.888 \times 10^{-10} T - 3.683 \times 10^{-13} T^2 + 1.548 \times 10^{-16} T^3} \quad (9)$$

with k = thermal diffusivity in m^2/s, T = temperature in °C, $r = 0.2$. Emissivity was fixed at 0.954 in the simulation and the temperature dependence of specific heat was considered according to thermodynamic data tables.[27] Radiative heat transfer between sample and furnace was approximated by:

$$\frac{dQ}{dt} = 4A\sigma\varepsilon T^3 \Delta T \quad (10)$$

with dQ/dt = heat flow, A = surface area, σ = Stefan Boltzmann constant, ε = emissivity, T = absolute temperature, ΔT = temperature difference between sample and furnace. The coefficient of heat transfer between sample and support was set to zero. The FE program ANSYS® (ANSYS Inc., Canonsburg, USA) was used with a cylindrical symmetry and element types PLANE55 and SURFACE151 for bulk and surface heat transfer, respectively. Equal temperatures of all inner surfaces of the furnace were assumed in the simulation. Furnace temperature was increased in small steps according to the specified heating rate. The time dependent temperature distribution of sample and holder was calculated subsequently.

3. Results and discussion

3.1. Sintering without load

Exemplarily, Fig. 3a shows the shrinkage curves of alumina green samples sintered without load at heating rates between 0.2 and 20 K/min. From the time derivatives of the shrinkage curves the respective true strain rates were calculated (compare Fig. 3b). Fig. 4 shows the corresponding kinetic field diagram where $\ln(-T d\varepsilon_f/dt)$ was plotted versus $1/T$. The iso-strain lines are labelled by the total shrinkage $\Delta L/L_0$ in Fig. 4 and all further kinetic field diagrams. Fig. 4a shows that the iso-strain lines bend towards higher temperatures at high heating rates (10 and 20 K/min). If only higher heating rates between 2 and 20 K/min are selected, straight lines can be fitted to the iso-strain lines (Fig. 4b). The range of heating rates between 0.2 and 2 K/min also led to straight iso-strain lines but the slope was larger (Fig. 4c).

Fig. 5 shows the activation energies derived from the slope of the respective iso-strain lines. An apparent activation energy of about 1000 kJ/mol was obtained for the smaller heating rates. A similar apparent activation energy for the densification in alumina of 1095 kJ/mol was reported recently, using similar heating

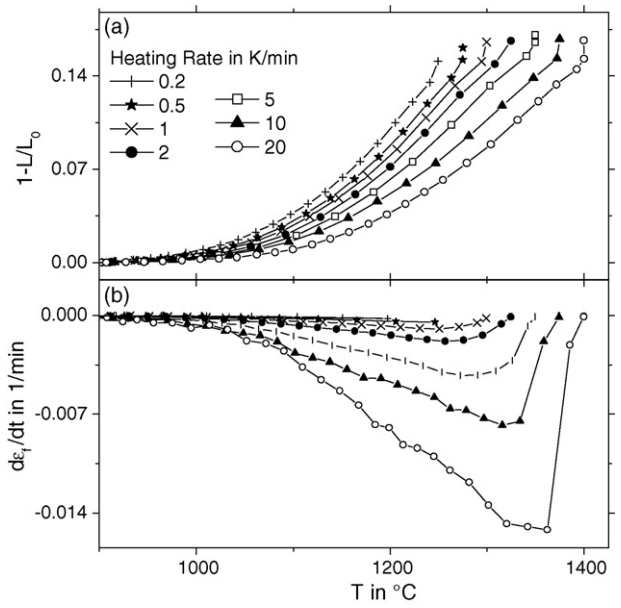

Fig. 3. Sintering shrinkage $1-L/L_0$ (a) and true strain rates $d\varepsilon_f/dt$ (b) of alumina green samples during heating with different constant heating rates without load.

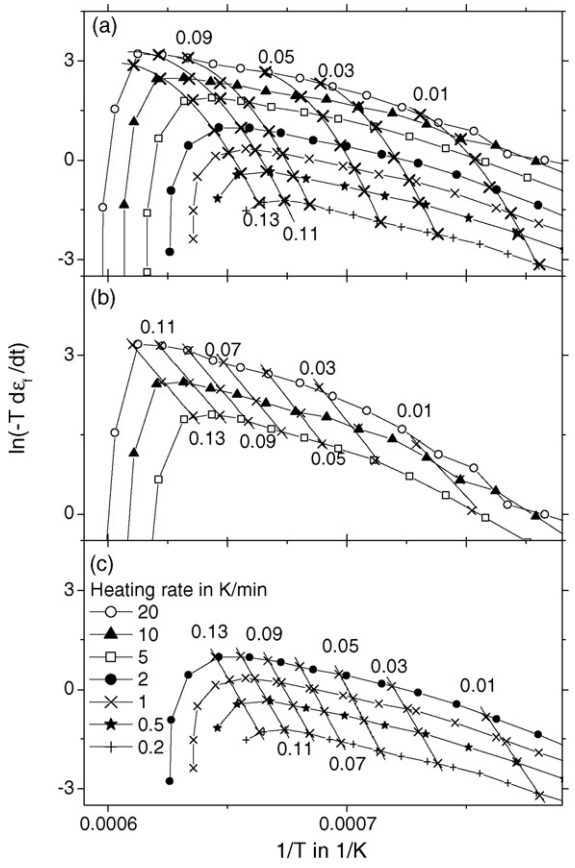

Fig. 4. Kinetic field diagram of the data from Fig. 3 with curved iso-strain lines (a); sections with heating rates between 5 and 20 K/min (b); and 0.2 and 2 K/min (c) showing straight iso-strain lines.

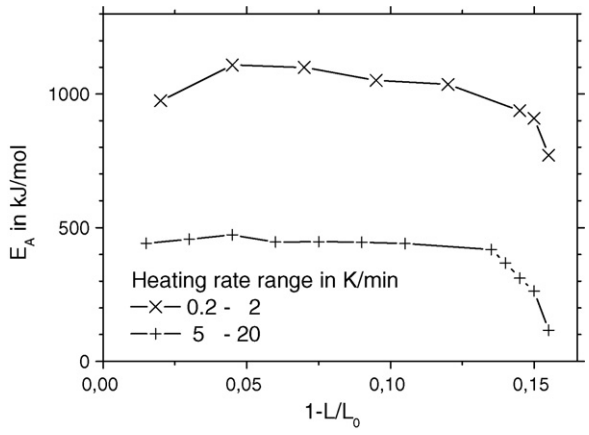

Fig. 5. Apparent activation energies during free sintering calculated from the slope of the iso-strain lines of Fig. 4b and c according to Eq. (6).

rates.[17] But the interpretation was different from ours – presented below. The apparent activation energy of 1000 kJ/mol was distinctly larger than the value of 580 kJ/mol reported for densification of alumina (compare Section 1). The discrepancy was attributed to coarsening which occurred simultaneously to shrinkage. From Eq. (5) it can be seen that grain growth leads to a decrease of shrinkage rate. This decrease shifts the iso-strain lines to higher temperatures, i.e. to the left in the kinetic field diagram. Without coarsening the strain rate curves should essentially follow the iso-strain lines since the first logarithm on the right hand side of Eq. (5) change only slightly with temperature. (At the end of sintering an additional shift of iso-strain lines towards higher temperature was expected from the decrease of strain rate when porosity approaches zero which is reflected in the constant $C_1(\rho)$ in Eq. (5)).

If the activation energy for the coarsening mechanism is smaller than the activation energy for densification, a clockwise rotation of the iso-strain lines and an increase of apparent activation energy are expected. This is caused by the relatively larger contribution of coarsening to microstructural changes at smaller heating rates, i.e. at lower temperatures, compared to larger heating rates. Coarsening retards shrinkage and shifts the next iso-strain point to higher temperatures, i.e. in the left direction in the kinetic field diagram. Since this shift is larger for smaller heating rates – still presumed that the activation energy for coarsening is smaller than for densification – the slope of the respective iso-strain line increases. Fig. 6 shows a fit of the parameters in Eqs. (2) and (5) to the iso-strain lines of Fig. 4c. With activation energies of 577 and 496 kJ/mol for sintering, respectively, grain growth, which were constant during the entire sintering cycle, a reasonable agreement to the experimental data was obtained. (The exponents n and m in Eqs. (1)–(3) were 3 and the initial grain size G_0 was 0.15 μm in the fit.) The fit demonstrated that the interplay of two mechanisms – densification and coarsening – with different activation energies led to completely different slopes. No new mechanisms as proposed in Ref. [17] are required to explain for the large apparent activation energies.

Fig. 5 shows that the apparent activation energy increased in the initial sintering stage. This was attributed to coarsening by surface diffusion of alumina. The activation energy of

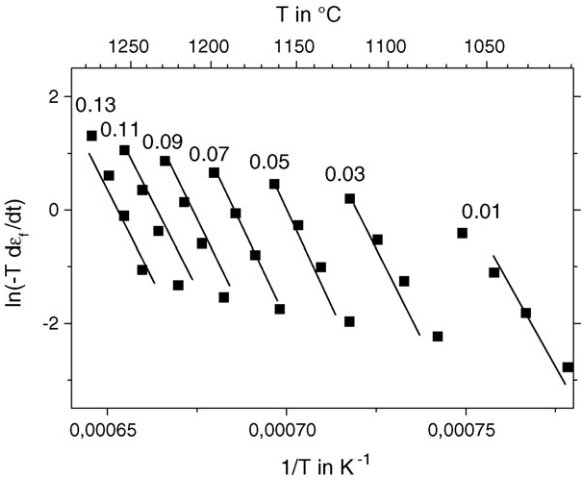

Fig. 6. Experimental iso-strain lines (straight lines) from Fig. 4c together with a fit of Eq. (5) to these lines (solid squares).

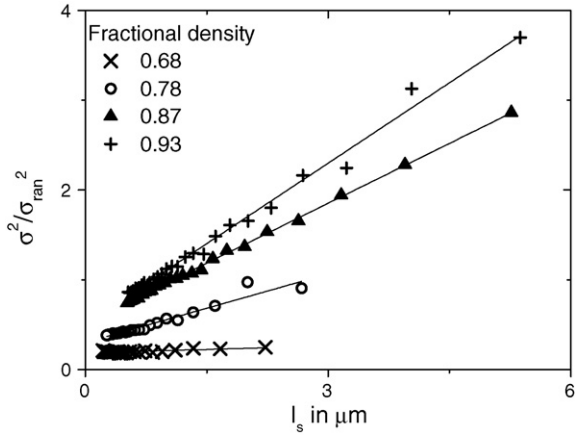

Fig. 8. Scaled variance σ^2/σ^2_{ran} versus edge length of corresponding sections l_s for partially sintered alumina samples.

about 250 kJ/mol is much smaller than that for lattice diffusion (compare Section 1) and should led to a clockwise rotation of the iso-strain lines. The constant apparent activation energy in the intermediate sintering stage (compare Fig. 5) and the larger activation energy of 496 kJ/mol for coarsening obtained from fitting the entire sintering cycle were explained by a change in the coarsening mechanism. It was assumed that preferential sintering within agglomerates led to local densification and lower density in the regions surrounding the agglomerates. This interpretation was supported by SEM analysis of quenched samples which showed an elimination of small intra-agglomerate pores (Fig. 7). Fig. 8 shows the scaled variance corresponding to the quenched samples of Fig. 7. Straight lines were fitted to the individual curves. The slope drastically increased with increasing density. This clearly demonstrated that homogeneity of the microstructure decreased during sintering. Although agglomeration was not considered in Eq. (1) it was assumed that it led to an increase of the denominator since grain size should be replaced by agglomerate size when the agglomerate fraction

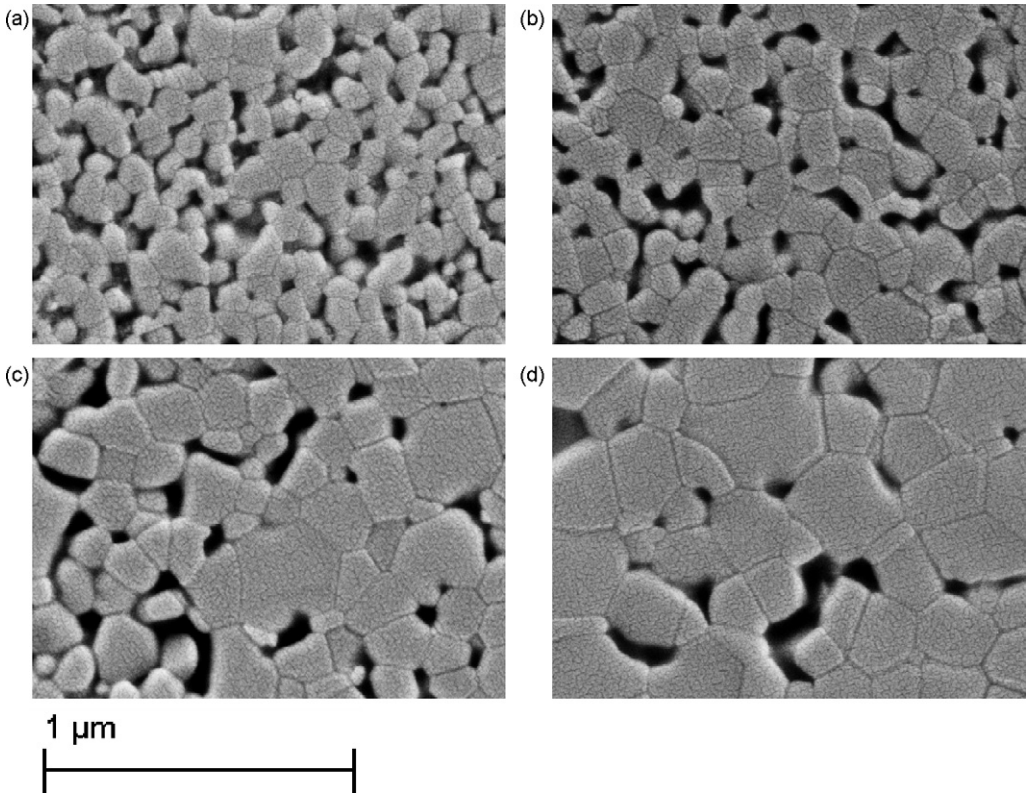

Fig. 7. SEM image of partially sintered alumina samples (heating rate 0.5 K/min) with fractional densities of 0.68 (a), 0.78 (b), 0.87 (c) and 0.93 (d).

became large and the shrinkage rate within the agglomerates small.

In the final sintering stage the accuracy of the activation energy data was worse because the small residual porosity led to a large decrease of strain rates. (Since the scaling of strains was done before the onset of shrinkage, errors may have accumulated during sintering.) Therefore, the data from Fig. 4c, reflecting heating rates between 0.2 and 2 K/min, were additionally evaluated in a different way using the measured final densities of the respective samples for a reverse scaling. Instead of iso-strain lines, iso-density lines were used in the kinetic field diagram. Fig. 9 shows the activation energies obtained from the slope of the iso-density lines in the final sintering stage. The decrease of apparent activation energy was confirmed. It was concluded that enhanced grain growth at higher heating rates and holding temperatures had occurred which had a larger activation energy than 580 kJ/mol. So it led to an anticlockwise rotation of the iso-strain and iso-density lines, respectively. Previous results on the activation energy for grain growth suggest that it decreases from 690 to 440 kJ/mol when porosity goes to zero (compare Section 1). This confirms that the activation energy for grain growth may be larger in the final sintering stage than that for densification. If so, grain growth can be reduced by decreasing the holding temperature in this period. The reduction of grain size at given density by applying a two step sintering process was demonstrated recently[28] and shows that a decrease of apparent activation energies at the end of sintering (compare Fig. 9) fits well to these results. In the initial sintering stage the increase in apparent activation energy suggests a fast heating if coarsening by surface diffusion shall be avoided. On the other hand, the subsequent coarsening by agglomeration can be reduced by an intense neck formation between the alumina particles which stabilises the microstructure and counteracts de-sintering.[29] This neck formation can be obtained by surface diffusion as well. It is enhanced by an additional holding period before the onset of shrinkage which has been suggested previously.[29,30] So there is a trade-off between avoiding coarsening and agglomeration. It was expected that different strategies are required even for a material as simple as alumina, depending on particle size distribution, impurities, dopants, green density and homogeneity of the green compacts. Especially, agglomeration during intermediate stage sintering which strongly depends on the forming process is believed to account for many discrepancies reported in the literature.

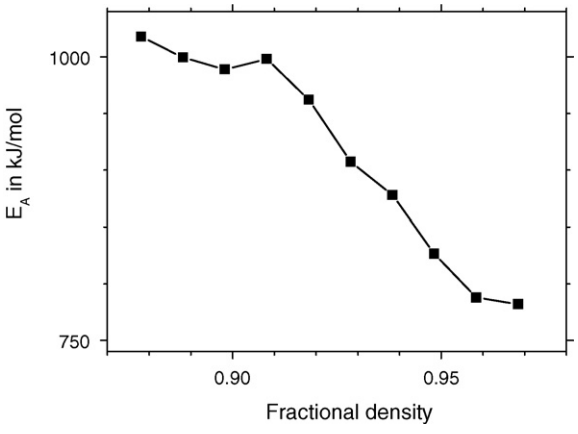

Fig. 9. Apparent activation energies in the final sintering stage for heating rates between 0.2 and 2 K/min derived from iso-density lines after reverse scaling with final densities.

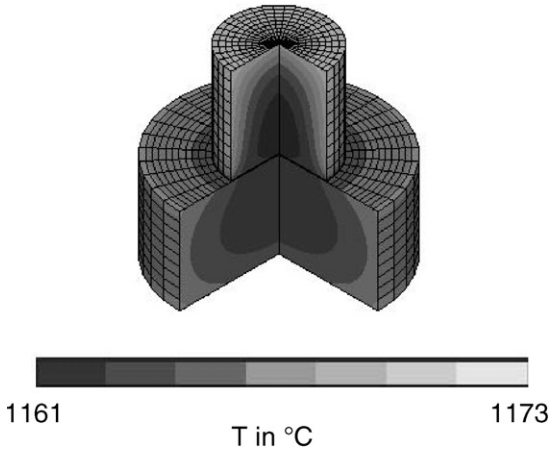

Fig. 10. Simulated temperature distribution within alumina sample after heating to 1175 °C at a heating rate of 20 K/min.

The bending of the iso-strain curves at high heating rates (compare Fig. 4a) was attributed to temperature gradients between furnace and sample during rapid heating. This was checked by an additional experiment where two pieces of gold sheet were placed in a hole drilled in the middle of the sample and on top of the sample, respectively. During heating with a heating rate of 20 K/min the gold sheet at the top melted at a furnace temperature of 1076 °C and the gold sheet in the centre at 1089 °C, i.e. 12 K, respectively, 25 K above its melting point of 1064 °C. From the FE simulation of the temperature gradients a temperature difference of 8 K was obtained for these two positions and the difference between sample centre and furnace was 13 K at a furnace temperature of 1175 °C and a heating rate of 20 K/min (Fig. 10). This was a reasonable agreement, considering the simplifications and the higher temperature in the simulation. The bending of the curves in Fig. 4a corresponded to a temperature shift of 20 K. It was concluded that temperature gradients can fully account for the bending phenomenon.

An apparent activation energy of 450 kJ/mol was derived for heating rates between 5 and 20 K/min (compare Fig. 5). Although this agreed well with 440 kJ/mol reported previously from constant heating rate sintering experiments on high purity alumina green samples where the same heating rates were used,[14] it was concluded that these results were falsified by the temperature gradients discussed above. So either a correction for temperature gradients has to be applied or heating rates have to be restricted to a range below 5 K/min. It was assumed that this is a general problem in studies of sintering kinetics at high heating rates. In the sinter forging experiments described in the next section, the later was done and heating rates were reduced to the range between 0.2 and 2 K/min.

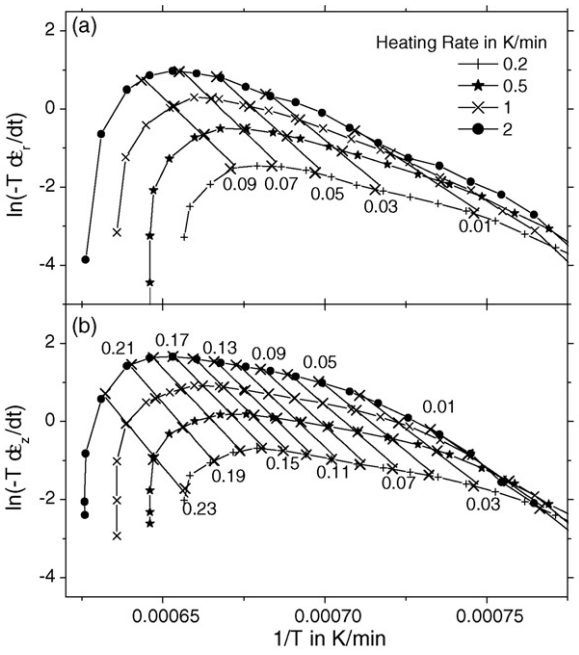

Fig. 11. Kinetic field diagrams of the axial (a) and lateral (b) strain rates measured during sinter forging with a constant load of 180 N.

3.2. Sintering with uni-axial loads

When uni-axial loads were applied, two different kinetic field diagrams were constructed for the strain rates parallel and perpendicular to the load, respectively. As an example, Fig. 11 shows these diagrams for a load of 180 N. The iso-strain lines for the axial strains were shifted towards lower, and the iso-strain lines for the lateral strains were shifted towards higher temperatures. The shift was caused by creep superposed to the sintering shrinkage (compare Eq. (3)). Kinetic field diagrams for different constant loads were assembled to a three dimensional figure with the load used as the z-axis. Iso-strain surfaces were constructed in 3d for each strain from the iso-strain lines of the individual kinetic field diagrams. This representation of the sintering data was called master sintering diagram (MSD). A contour plot of the iso-strain surfaces is shown in Fig. 12. It can be seen from Fig. 12b that already at 1% axial strain a large shift of the iso-strain lines with increasing load was obtained. This was attributed to the large stress intensification at the small particle contacts in the initial sintering stage. Remarkably the iso-strain lines belonging to the same strain remained parallel when a load was applied (compare Fig. 12). The simple structure of the MSD reflects the similar mechanisms which control creep and sintering. If the activation energies for densification and creep Q and Q_c are identical, Eqs. (1) and (4) can be substituted in Eq. (3):

$$\ln\left(-T\frac{\mathrm{d}\varepsilon_z}{\mathrm{d}t}\right) = \ln(C_4(\rho, G) - C_5(\rho, G)) - \frac{Q}{R}\frac{1}{T};$$
$$\ln\left(-T\frac{\mathrm{d}\varepsilon_r}{\mathrm{d}t}\right) = \ln(C_4(\rho, G) + C_5(\rho, G)\nu_v) - \frac{Q}{R}\frac{1}{T};$$
$$\text{with } C_4(\rho, G) = \frac{C_1(\rho)\gamma D_0}{kG^n}; C_5(\rho, G) = \frac{\sigma_Z C_3(\rho)}{kG^p} \quad (11)$$
$$\text{with } C_4(\rho, G) = \frac{C_1(\rho)\gamma D_0}{kG^n}; \quad C_5(\rho, G) = \frac{\sigma_Z C_3(\rho)}{kG^p}$$

Note that σ_z was negative so that the increase of $-\mathrm{d}\varepsilon_z/\mathrm{d}t$ and the decrease of $-\mathrm{d}\varepsilon_r/\mathrm{d}t$ were also confirmed by Eq. (11). $C_5(\rho, G)$ shows only a small variation with temperature in the initial and intermediate sintering stage. Note that unlike sintering

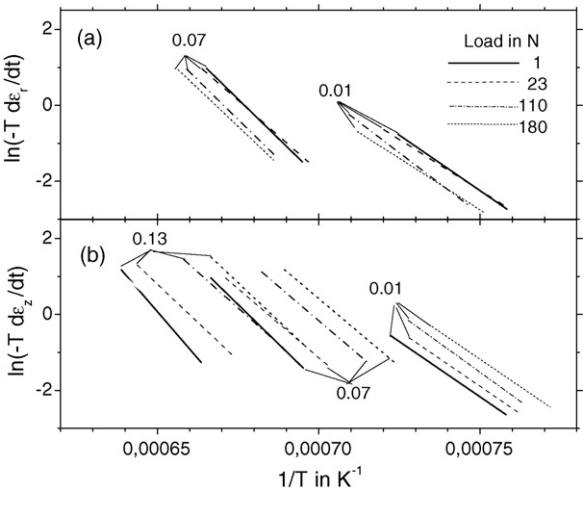

Fig. 12. Section of the Master Sintering Diagram (MSD): contour plot of various lateral (a) and axial (b) iso-strain surfaces at different loads.

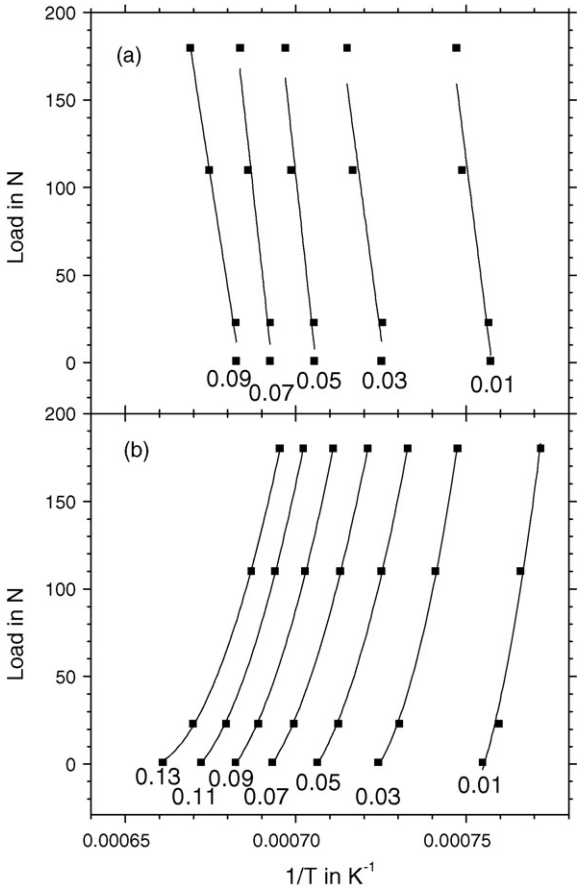

Fig. 13. Section of the MSD: cut through iso-strain surfaces at $\ln(-T\,\mathrm{d}\varepsilon/\mathrm{d}t) = 0$.

shrinkage creep is more controlled by the grain size than by the size of the agglomerates. Therefore, a parallel shift of the iso-strain lines is expected from Eq. (11) when the load is varied. The same parallel shift of iso-strain lines was recently measured for zirconia.[31] For the numeric representation of the MSD, the average slope obtained for different loads at each iso-strain line was used. The shift of the iso-strain lines with increasing load was fitted by low order polynomials to construct the iso-strain surfaces. Fig. 13 shows a vertical cut through the MSD at $\ln(-T\mathrm{d}\varepsilon/\mathrm{d}t) = 0$. The iso-strain surfaces for the lateral strain could be fitted by linear equations whereas the effect of load on axial strain was larger and the corresponding iso-strain surfaces showed a convex curvature (compare Fig. 13). Using the MSD axial and lateral strain rates could be calculated for arbitrary constant heating rates and constant loads within the range of the experiments underlying the MSD. Presently loading history prevents accurate prediction of strain rates at non-constant heating rates and loads by the MSD. To consider these loading memory effects, cyclic loading experiments were performed which are described in a subsequent paper.[31]

4. Conclusions

Kinetic field diagrams can be used to identify mechanisms interacting indirectly with shrinkage, e.g. surface diffusion, agglomeration and grain growth. The shift and the rotation of the iso-strain lines in the kinetic field provide information on the extent of coarsening and the related activation energy compared to the activation energy for densification. If the activation energy for the coarsening mechanism is smaller than for densification, a clockwise rotation of the iso-strain lines is obtained and vice versa a counterclockwise rotation. So from plotting the kinetic field diagram an immediate decision can be made whether sintering at high or low temperatures is better to enhance densification versus coarsening. This allows the construction of improved temperature cycles.

In the present investigation a large effect of temperature gradients was detected from the bending of iso-strain lines in the kinetic field. It was concluded that temperature gradients have to be considered for a sample size above 1 cm and a heating rate above 5 K/min. The threshold values are reduced if ceramic with lower thermal diffusivity than alumina (e.g. zirconia) is investigated.

A master sintering diagram was composed from different kinetic field diagrams using the load as z-axis. Iso-strain surfaces were constructed, which are a 3d extension of the iso-strain line concept. The individual iso-strain lines showed a parallel shift in the x–y plane with increasing load. This enabled a rather simple geometry of the iso-strain surfaces representing the entire information on the effects of load, temperature, heating rate and porosity on densification.

Acknowledgements

The authors acknowledge the help of H. Schömig, R. Winter, M. Römer and A. Streltsov with sample preparation and measurements.

References

1. Riedel, H., Zipse, H. and Svoboda, J., Equilibrium pore surfaces, sintering stresses and constitutive equations for the intermediate and late stages of sintering. II. Diffusional densification and creep. *Acta Metall. Mater.*, 1994, **42**, 445–452.
2. Camacho-Montes, H., Garcia-Casillas, P. E., Rodriguez-Ramos, R., Fuentes-Montero, M. E. and Fuentes-Cobas, L. E., Simulation of the stress-assisted densification behavior of powder compact: effect of constitutive law. *J. Am. Ceram. Soc.*, 2008 [online early articles].
3. Aulbach, E., Zuo, R. and Rödel, J., Laser-assisted high-resolution loading dilatometer and applications. *Exp. Mech.*, 2004, **44**, 71–75.
4. Cai, P. Z., Messing, G. L. and Green, D. L., Determination of the mechanical response of sintering compacts by cyclic loading dilatometry. *J. Am. Ceram. Soc.*, 1997, **82**, 445–452.
5. Zuo, R., Aulbach, E. and Rödel, J., Viscous Poison's coefficient determined by discontinuous hot forging. *J. Mater. Res.*, 2003, **18**, 2170–2176.
6. Rahaman, M. N., *Sintering of Ceramics*. CRC Press, Boca Raton, 2008.
7. Coble, R. L., A model for boundary diffusion controlled creep in polycrystalline materials. *J. Appl. Phys.*, 1963, **34**, 1679–1682.
8. Herring, C., Diffusional viscosity of a polycrystalline solid. *J. Appl. Phys.*, 1950, **21**, 437–445.
9. Dillon, S. J. and Harmer, M. P., Intrinsic grain boundary mobility in alumina. *J. Am. Ceram. Soc.*, 2006, **89**, 3885–3887.
10. Su, H. and Johnson, D. L., Master sintering curve: a practical approach to sintering. *J. Am. Ceram. Soc.*, 1996, **79**, 3211–3217.
11. Kiani, S., Pan, J. and Yeomans, J. A., A new scheme of finding the master sintering curve. *J. Am. Ceram. Soc.*, 2006, **89**, 3393–3396.
12. An, K. and Johnson, D. L., The pressure-assisted master sintering surface. *J. Mater. Sci.*, 2002, **37**, 4555–4559.
13. Palmour III, H., Rate-controlled sintering technology for PM and composites. *Powder Metal Rep.*, 1988, **9**, 572–579.
14. Wang, J. and Raj, R., Estimate of the activation energies for boundary diffusion from rate-controlled sintering of pure alumina, and alumina doped with zirconia or titania. *J. Am. Ceram. Soc.*, 1990, **73**, 1172–1175.
15. Raether, F., Current state of in-situ measuring methods for the control of firing processes. *J. Am. Ceram. Soc.*, 2009, **92**, 146–152.
16. Zimmer, J., Raether, F., Jaenicke-Rößler, K. and Leitner, G., A system for rate controlled sintering by kinetic field approach. In *Ceramics: Getting into the 2000's – Part B*, ed. P. Vincenzini. Techna Srl., 1999, pp. 693–702.
17. Bernard-Granger, G., Guizard, C. and Addad, A., Sintering of an ultra pure α-alumina powder: I. Densification, grain growth and sintering path. *J. Mater. Sci.*, 2007, **42**, 6316–6324.
18. Xue, L. A., Chen, I.-W. and Deformation, Grain Growth of low-temperature-sintered high-purity alumina. *J. Am. Ceram. Soc.*, 1990, **73**, 3518–3521.
19. Bae, S. I. and Baik, S., Sintering and grain growth of ultrapure alumina. *J. Mater. Sci.*, 1993, **28**, 4197–4202.
20. Shaw, N. J. and Brook, R. J., Structure and grain coarsening during the sintering of alumina. *J. Am. Ceram. Soc.*, 1986, **69**, 107–110.
21. Zuo, R., Aulbach, E., Bordia, R. K. and Rödel, J., Critical evaluation of hot forging experiments: case study in alumina. *J. Am. Ceram. Soc.*, 2003, **86**, 1099–1105.
22. Missiaen, J.-M. and Thomas, G., Homogeneity characterization of binary grain mixtures using a variance analysis of two-dimensional numerical fractions. *J. Phys. Condens. Matter*, 1995, **7**, 2937–2948.
23. Raether, F., Springer, R. and Beyer, S., Optical dilatometry for the control of microstructure development during sintering. *Mater. Res. Innovat.*, 2001, **4**, 245–250.
24. Nielsen, T. and Leipold, M., Thermal expansion in air of ceramic oxides to 2200 °C. *J. Am. Ceram. Soc.*, 1963, **46**, 381–387.
25. Wachtmann, J. B., Scuderi, T. and Cleek, G., Linear thermal expansion of aluminum oxide and thorium oxide from 100 to 1100 K. *J. Am. Ceram. Soc.*, 1962, **45**, 319–323.
26. Raether, F., Hofmann, R., Müller, G. and Sölter, H. J., A novel thermo-optical measuring system for the in situ study of sintering processes. *J. Therm. Anal. Calorim.*, 1998, **53**, 717–735.

27. Barin, I., *Thermochemical Data of Pure Substances*. VCH Verlagsgesellschaft, Weinheim, Germany, 1989.
28. Bodisova, K. and Sajgalik, P., Two-stage sintering of alumina with submicrometer grain size. *J. Am. Ceram. Soc.*, 2007, **90**, 330–332.
29. Raether, F., Zimmer, J. and Springer, R., Improved sintering of alumina by new in situ measuring methods. In *Ceramics: Getting into the 2000's – Part B*, ed. P. Vincenzini. Techna Srl., 1999, pp. 711–720.
30. Chu, M.-Y., De Jonghe, L. C., Lin, M. K. F. and Lin, F. J. T., Precoarsening to improve microstructure and sintering of powder compacts. *J. Am. Ceram. Soc.*, 1991, **74**, 2902–2911.
31. Delporte, M., Raether, F., Eisele, U., Measurement of sintering kinetics and viscous moduli for PSZ using combined master sintering diagram and cyclic loading. *J. Am. Ceram. Soc*., submitted for publication.